Materials Advances

ROYAL SOCIETY OF CHEMISTRY

PAPER

View Article Online
View Journal | View Issue

Check for updates

Cite this: *Mater. Adv.*, 2022, 3, 5055

Relating the structure, properties, and activities of nanostructured $SrTiO_3$ and $SrO-(SrTiO_3)_n$ (n = 1 and 2) for photocatalytic hydrogen evolution†

Aditi Vijay, Kadambari Bairagi and Sonalika Vaidya *

Received 28th January 2022,
Accepted 25th April 2022

DOI: 10.1039/d2ma00097k

rsc.li/materials-advances

This study focuses on relating the structure of perovskite oxides with their properties and activities and provides a comparative study of the three members of the Sr–Ti–O system for photocatalytic hydrogen evolution. The three oxides focused on in this study are based on perovskite structure *viz.* $SrTiO_3$ and $SrO-(SrTiO_3)_n$ (n = 1 and 2). We have successfully synthesized these three oxides through a methodology that combined the polymeric citrate precursor method with the hydrothermal method. Their crystal structure, morphology, and optical properties (absorption and photoluminescence) were systematically explored. $SrTiO_3$ belonged to a class of cubic perovskite while Sr_2TiO_4 (n = 1) and $Sr_3Ti_2O_7$ (n = 2) belonged to layered Ruddlesden–Popper based perovskite oxides. We observed the cube-shaped morphology for nanostructured $SrTiO_3$ and layered morphology for Ruddlesden–Popper based oxides, Sr_2TiO_4 and $Sr_3Ti_2O_7$. The photocatalytic hydrogen evolution performance of these nanostructured oxides was investigated. Amongst the three nanostructured oxides, the maximum amount of hydrogen was evolved with $Sr_3Ti_2O_7$ as the photocatalyst. These results were supported by photoluminescence, time-resolved photoluminescence, and photoelectrochemical studies.

1. Introduction

Production of hydrogen energy *via* the utilization of solar energy is a sustainable and effective solution to the world's energy crisis and environmental problems. In this regard, photocatalytic splitting of water into H_2 and O_2 over a semiconducting catalyst has been recognized as an effective strategy to develop a sustainable energy structure.[1,2] The efficiency of a photocatalytic reaction can be enhanced by modulating several factors such as crystal structure,[3] electronic structure[4] (*i.e.* position of the conduction band and valence band edge), the presence of vacancies (anion or cation)[5] and controlling the morphology.[6,7]

Over the past few decades, several semiconductor oxides such as TiO_2, ZnO, $AgGaO_2$, and $BiVO_4$ have been discovered as efficient catalysts for photocatalytic hydrogen evolution.[8–14] Among all the developed photocatalysts, perovskite structures *i.e.* ABO_3 have gained much popularity because of their composition which can be easily modulated at A and B sites.[15–17] Among the various perovskite semiconductor oxides, $SrTiO_3$ is widely studied as a photocatalyst[18–20] for its outstanding structural stability and compositional flexibility. Ruddlesden Popper-based layered perovskites, with a general formula of $AO-(ABO_3)_n$, (which can be also written as $(A_{n+1}BO_{3n+1})$ or $A'_2[A_{n-1}B_nO_{3n+1}]$) have attracted much attention in the field of photocatalytic water splitting due to their physical properties which can be modified by intercalation and ion-exchange.[21,22] These structures consist of a large number of active sites such as the B site and the AO layer site to facilitate the reaction. Several metal ions can be doped[23,24] at the A and B sites in these structures which modulates the bandgap of the oxide towards the visible region thereby enhancing their photocatalytic activity.

Fig. 1 shows the crystal structure of $SrTiO_3$ and $SrO-(SrTiO_3)_n$ (n = 1 and 2). $SrTiO_3$ belongs to the class of perovskite that has a cubic structure composed of corner shared TiO_6 octahedra with Sr, present in the holes formed from the cuboctahedron symmetry. When n = 1 and 2, the structure belongs to a class of oxide known as Ruddlesden–Popper phases. The two-lower symmetry 2D-Ruddlesden–Popper oxides, Sr_2TiO_4 (n = 1) and $Sr_3Ti_2O_7$ (n = 2) have body-centered tetragonal symmetry. These structures are composed of stacked $n SrTiO_3$ perovskite layers separated by a SrO rock-salt type layer, as shown in Fig. 1.

Here, we discuss a comparative study of the performance of nanostructured $SrTiO_3$ and $SrO-(SrTiO_3)_n$ *viz.* Sr_2TiO_4 (n = 1) and $Sr_3Ti_2O_7$ (n = 2) towards photocatalytic hydrogen evolution reactions. Out of these three perovskite oxides, Sr_2TiO_4 and $Sr_3Ti_2O_7$ belong to $I4/mmm$, tetragonal symmetry whereas $SrTiO_3$ belongs to the $Pm\bar{3}m$ space group. The photocatalytic

---

Institute of Nano Science and Technology, Knowledge City, Sector 81, Sahibzada Ajit Singh Nagar, Punjab 140306, India. E-mail: svaidya@inst.ac.in

† Electronic supplementary information (ESI) available. See DOI: https://doi.org/10.1039/d2ma00097k

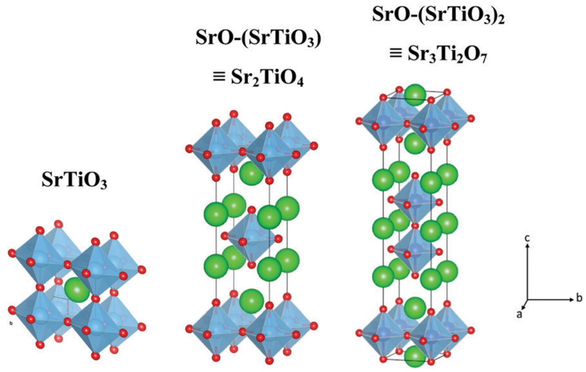

Fig. 1 Schematic showcasing the crystal structure of $SrTiO_3$ and SrO–$(SrTiO_3)_n$ for $n = 1$ (Sr_2TiO_4) and $n = 2$ ($Sr_3Ti_2O_7$).

property of these nanostructured oxides is investigated through hydrogen evolution reactions under UV-visible light irradiation. Photoluminescence, time-resolved photoluminescence, and photoelectrochemical studies have been carried out to see the role of the perovskite structure in influencing photocatalytic activity. To the best of our knowledge, there are no reports on a comparative study of the three kinds of structures on photocatalytic hydrogen evolution performance. However, there is one report[25] where the ratio of Sr/Ti in $SrTiO_3$ was varied and their photocatalytic HER was studied for different ratios from 1.00 to 1.25. The photocatalytic hydrogen evolution activity of these three perovskite oxides has been studied separately.[26–28] In this study, we have tried to highlight that the choice of structure (crystallographic), amongst the cubic and layered perovskites (showcased here with the Sr–Ti–O system), could be an efficient way for the development of a catalyst for a hydrogen evolution reaction with improved performance.

2. Experimental

2.1 Materials and methods

Strontium nitrate [($Sr(NO_3)_2$), 99%], ethylene glycol (EG) (99%), methanol (ACS grade), citric acid anhydrous (98%), and sodium sulfate (99%) were purchased from Merck. Sodium sulfide flakes were purchased from CDH fine chemicals. Titanium tetraisopropoxide (TTIP) (97%) and sodium sulfite (98%) were purchased from Sigma-Aldrich.

For the synthesis of $SrTiO_3$, TTIP (12 mmol) was added to a mixture of ethylene glycol (25 mL) and methanol (10 mL). To this aqueous solution of citric acid in 5 mL water and solid $Sr(NO_3)_2$ (12 mmol) were added. The amount of citric acid taken was equivalent to that of TTIP. The resultant mixture was heated at 130 °C for 4 hours to form a single-phase transparent solution. Afterward, the pH of this solution was adjusted to 13 by adding 5 M NaOH (5 mL). The resulting solution was transferred into a Teflon vessel followed by hydrothermal treatment at 200 °C for 48 h. After the Teflon vessel was cooled down to room temperature, the obtained gel was vacuum dried at 200 °C for 16 h. The products were washed several times with glacial acetic acid (to remove carbonate present as an impurity in the sample), deionized (DI) water, and ethanol, and then dried overnight at 70 °C. $SrTiO_3$ was finally synthesized by calcining the dried powder at 750 °C for 5 h.

For the synthesis of Sr_2TiO_4 and $Sr_3Ti_2O_7$, the exact procedure was followed as for $SrTiO_3$ except for the ratio of Sr and Ti precursor and heating temperature. For Sr_2TiO_4, the ratio of Sr and Ti precursor was kept at 2 : 1 (12 mmol of $Sr(NO_3)_2$ and 6 mmol of TTIP) and calcined first at 650 °C and then at 1000 °C for 12 h, whereas for $Sr_3Ti_2O_7$ the ratio was kept at 3 : 2 (9 mmol of $Sr(NO_3)_2$ and 6 mmol of TTIP) and calcined first at 650 °C and then at 950 °C for 6 h.

2.2 Characterization

Phase identification and crystal structure of the samples were analyzed using powder X-ray diffraction (PXRD, Bruker D8 Advance Eco) with Cu Kα as an X-ray source (λ = 0.15406 nm). The step size of 0.02 with a time of 0.3 s per step was used for data collection. Crystallite size (Scherrer) was calculated using TOPAS v5 software by using the peak positioned at a two-theta value of 32.5°, 31.4°, and 46.6° for $SrTiO_3$, Sr_2TiO_4, and $Sr_3Ti_2O_7$ respectively. To obtain information about the morphology of the sample, transmission electron microscopy studies were carried out on a JEOL, JEM-2100 Transmission Electron Microscope (TEM), used at an operating voltage of 200 kV. The samples for the TEM study were prepared by dispersing the powder samples in ethanol and drop-casting them on a carbon-coated copper grid. Raman study was carried out on a WI Tec's Raman microscope, α 300 R. The studies were carried out on powder samples taken on a glass slide. Diffuse Reflectance Spectra were collected on a UV-visible spectrophotometer, Shimadzu UV-2600, in a wavelength range of 200–800 nm with barium sulfate as the reference material. Kubelka–Munk's (K–M) equation was used to calculate the band-gap of the materials from the reflectance spectra. XPS (X-Ray Photoelectron Spectroscopy) studies were carried out on a Thermo Scientific's K-alpha X-ray Photoelectron Spectrometer (XPS) System with the following settings: 0.05 eV step, 1 s time per step, and 5 cycles, Source Al k-alpha-1486 eV. The surface area of the samples was determined using nitrogen adsorption–desorption isotherms with Quanta Chrome Model Q2. Photoluminescence and time-resolved photoluminescence spectra were obtained from Horiba's TCSPC (Time Correlated Single Photon Counting) at an excitation wavelength of 380 nm and 340 nm respectively. Time-resolved photoluminescence decay curves were fitted by using a double logarithmic decay equation which is given below:

$$y = A_1 e^{(-x/\tau_1)} + A_2 e^{(-x/\tau_2)} + y_0 \tag{1}$$

The average lifetime was obtained from the equation given below:

$$\tau = \frac{\sum_{i=1}^{n} A_i \tau_i^2}{\sum_{i=1}^{n} A_i \tau_i} \tag{2}$$

2.2.1 Photocatalytic hydrogen evolution reaction (HER) and photoelectrochemical studies. A top irradiation quartz reactor of capacity 140 mL was used for the photocatalytic reaction for the hydrogen evolution. In a typical experiment, 40 mg of the catalyst were dispersed in a 40 mL aqueous solution containing 0.35 M Na_2SO_3 and 0.25 M Na_2S through ultrasonication. The study was carried out in the absence of any metal co-catalyst to observe the direct influence of the nature of the crystal structure on the photocatalytic performance of Sr–Ti–O based oxides. The solution was purged with N_2 gas for 30 minutes to eliminate the dissolved oxygen. A 450 W Xe lamp was used as a source of light. The photon flux of the Xe lamp was obtained from Ray virtual radiation actinometer, Newport, Model 91150V. The gas components from the reactor were analyzed using gas chromatography (GC, PerkinElmer Clarus 680) with a thermal conductivity detector at an interval of 1 h. The apparent quantum efficiency was calculated using the equation given below:

$$\mathrm{AQY} = \frac{2nN_{\mathrm{A}}hc}{PS\lambda t} \times 100 \tag{3}$$

where n is the amount of hydrogen evolved; N_A is Avogadro's constant (6.022×10^{23} mol^{-1}); h is Planck's constant (6.63×10^{-34} J s); c is the speed of the light (3×10^{10} cm s^{-1}); P is the power density of the incident light (181×10^{-3} W cm^{-2}); S is the irradiation area (12.6 cm^2); λ is the representative wavelength of the incident light (using the radiation spectrum of the Xenon lamp, 390 nm (390×10^{-7} cm)); and t is the time duration of the incident light (18000 s).

Photoelectrochemical studies were performed on a PGSTAT-30 (Autolab) electrochemical workstation using a standard three-electrode system consisting of Ag/AgCl (3 M KCl) as the reference electrode, platinum wire as the counter electrode, and Sr–Ti–O samples deposited on a glass substrate coated with fluorine-doped tin oxide (FTO) as the working electrode. For the synthesis of the working electrode, the catalyst was drop cast on a glass substrate coated with FTO with an area of 1 cm × 1 cm. For the preparation of the catalyst ink, 10 mg of the catalyst was dispersed in 200 μL of isopropyl alcohol containing 10 μL of Nafion resin solution through the ultra-sonication method. Here, 0.1 M Na_2SO_4 (pH = 7) was taken as an electrolyte, and saturated with argon for 30 minutes to remove dissolved oxygen. A 350 W Xe lamp was used as the source of irradiation. LSV (linear sweep voltammetry) curves were obtained in the range from 0 to −1 V *vs.* Ag/AgCl at a scan rate of 10 mV s^{-1} under the light. Electrochemical impedance spectroscopy (EIS) was carried out at −0.35 V *vs.* Ag/AgCl in the frequency range from 0.1 Hz to 100 kHz under light.

3. Results and discussion

The powder X-ray diffraction (PXRD) pattern of the as-prepared nanostructured oxides is shown in Fig. 2. No impurity peaks were observed in the PXRD pattern indicating the formation of a single phase. The pattern for the perovskite $SrTiO_3$ was indexed based on cubic symmetry (PDF 00-035-0734, space group, $Pm\bar{3}m$). The other two Ruddlesden–Popper layered structures, Sr_2TiO_4 (n = 1) and $Sr_3Ti_2O_7$ (n = 2) were indexed based on tetragonal symmetry with the space group, $I4/mmm$ (JCPDF 00-039-1471 and JCPDF 01-078-2479 respectively). The crystallite sizes for all three oxides *viz.* $SrTiO_3$, Sr_2TiO_4, and $Sr_3Ti_2O_7$ were found to be 63 nm, 39 nm, and 42 nm respectively.

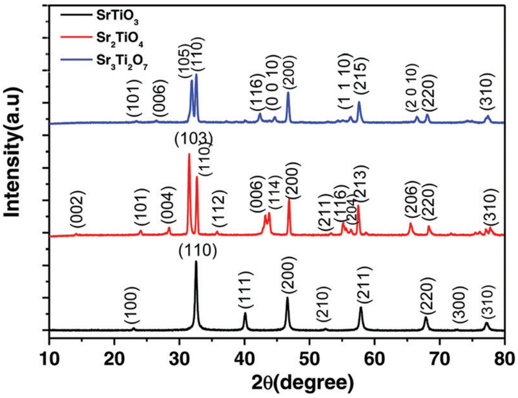

Fig. 2 PXRD pattern for $SrTiO_3$, Sr_2TiO_4, and $Sr_3Ti_2O_7$.

Raman spectra of the three nanostructured oxides *i.e.* $SrTiO_3$, Sr_2TiO_4, and $Sr_3Ti_2O_7$ are shown in Fig. 3. The Raman spectra obtained for the perovskite $SrTiO_3$ matched well with the previous reports.[29,30] The spectra consist of a low-frequency band present at 77 cm^{-1} which was assigned to doubly degenerate modes, E_g. Second order Raman bands were also observed between 200–400 cm^{-1} and 600–800 cm^{-1}. No first-order bands were observed in the Raman spectra, as expected for the cubic structure. According to the report by Nilsen *et al.*[29] second-order Raman scattering is due to the creation and destruction of two phonons which can originate from anywhere in the Brillouin zone. The authors observed a second-order band or overtone for $SrTiO_3$ at 369 cm^{-1} which was attributed to the combination of various bands including the TO_4–TA, TO_4–TO_l, and $2TO_2$ bands whereas the band at 684 cm^{-1} was assigned to the $2TO_3$ overtone. It has been previously reported[31] that there are four Raman active modes, A_{1g}, and E_g, observed for layered Ruddlesden–Popper oxides with n = 1, Sr_2TiO_4. The Raman bands present at 121, 203, 182, and 571 cm^{-1} were assigned to the E_g, A_{1g}, E_g, and A_{1g} modes respectively (Fig. 3). The broader band observed between 400–450 cm^{-1} and around 700 cm^{-1} indicates the presence of a second-order band or defect-induced

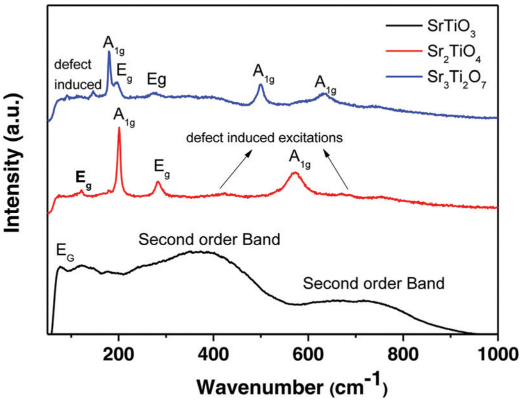

Fig. 3 Raman spectra of $SrTiO_3$, Sr_2TiO_4, and $Sr_3Ti_2O_7$.

excitations which may originate at the oxygen sublattice. The Raman spectra of $Sr_3Ti_2O_7$ (Fig. 3) show bands at 178, 198, 274, 500, and 633 cm^{-1} which can be assigned to the A_{1g}, E_g, E_g, A_{1g}, and A_{1g} modes respectively which is consistent with a previous report.[32] A defect-induced excitation was also observed at 92 cm^{-1}. The band corresponding to the A_{1g} mode was observed to be more intense in both Sr_2TiO_4 and $Sr_3Ti_2O_7$, which could be due to symmetric stretching of the oxygen lattice.[33]

The high resolution XPS spectra of strontium (Sr(3d), Fig. S1a–c, ESI†), oxygen (O(1s), Fig. S2a–c, ESI†) and titanium, (Ti(2p), Fig. S3a–c, ESI†), was obtained for $SrTiO_3$ Sr_2TiO_4 and $Sr_3Ti_2O_7$. Peaks at binding energies of 133.7 eV (135.5 eV), 133.9 eV (135.5 eV) and 133.6 eV (135.4 eV) were observed in the Sr $3d_{5/2}$ ($3d_{3/2}$) spectra of $SrTiO_3$ (Fig. S1a, ESI†), Sr_2TiO_4 (Fig. S1b, ESI†) and $Sr_3Ti_2O_7$ (Fig. S1c, ESI†) respectively. Fig. S2a–c (ESI†) show the high-resolution O 1s spectra for $SrTiO_3$, Sr_2TiO_4, and $Sr_3Ti_2O_7$. The peaks were fitted with two Gaussian peaks with binding energies at 529.7 and 531.2 eV for $SrTiO_3$, 529.3 and 531.4 eV for Sr_2TiO_4 and 529.8 and 531.77 eV for $Sr_3Ti_2O_7$. The peak at lower energy can be attributed to the metal–oxygen bond *i.e.* the presence of O^{2-} ions in the crystal structure whereas the peak at higher energy can be related to the oxygen vacancies. Fig. S3a–c (ESI†) shows the high-resolution spectra of Ti(2p) for $SrTiO_3$, Sr_2TiO_4, and $Sr_3Ti_2O_7$ respectively. The presence of Ti^{3+} was observed along with the Ti^{4+} ion after fitting of the peaks. The peaks centered at 458.3 eV (464.2 eV), 458.1 eV (453.8 eV) and 458.5 eV (464.1 eV) were observed for the Ti^{4+} $2p_{3/2}$ ($2p_{1/2}$) spectra of $SrTiO_3$, Sr_2TiO_4 and $Sr_3Ti_2O_7$ respectively. Ti^{3+} $2p_{3/2}$ ($2p_{1/2}$) spectra of $SrTiO_3$, Sr_2TiO_4 and $Sr_3Ti_2O_7$ were obtained at 456.4 eV (462.8 eV), 456.8 eV (462.1 eV) and 456.6 eV (461.9 eV) respectively. Thus the presence of peaks corresponding to Ti^{3+} also confirms the presence of an oxygen vacancy in the lattice. Based on the area under the peak, the order for the ratio of oxygen vacancies : M–O and Ti^{3+}:Ti^{4+} was found to be $Sr_2TiO_4 > Sr_3Ti_2O_7 > SrTiO_3$.

TEM studies for $SrTiO_3$ showed nanocubes with a size of 80–100 nm (Fig. 4a). The HRTEM image (Fig. 4b) shows lattice fringes with a spacing of 0.281 nm, corresponding to the (110) plane. A rectangular sheet-like morphology was observed for both Ruddlesden–Popper based oxides *i.e.* Sr_2TiO_4 (Fig. 4c) and $Sr_3Ti_2O_7$ (Fig. 4e). The size along one dimension of these sheets was observed to be ~250 nm and ~350 nm for Sr_2TiO_4 and $Sr_3Ti_2O_7$ respectively. The lattice fringes corresponding to a spacing of 0.276 nm for Sr_2TiO_4 (Fig. 4d) and 0.273 nm for $Sr_3Ti_2O_7$ (Fig. 4f) were observed which corresponded to the (110) plane. The BET surface area of all the samples *viz.* $SrTiO_3$, Sr_2TiO_4, and $Sr_3Ti_2O_7$ were observed to be 15 m^2 g^{-1}, 6.2 m^2 g^{-1}, and 14 m^2 g^{-1} respectively.

The bandgap of the oxides was calculated using the Tauc equation (eqn (4)).

$$(\alpha h\upsilon)^{\frac{1}{n}} = C\left(h\upsilon - E_g\right) \qquad (4)$$

where E_g is the bandgap of the semiconductor materials; h is Planck's constant, υ is the frequency of the light, α is the absorption coefficient; n represents the type of transition ($n = \frac{1}{2}$ stands for direct transition whereas $n = 2$ is used for indirect transition). It is known that the oxides *viz.* $SrTiO_3$, Sr_2TiO_4 and $Sr_3Ti_2O_7$ possess an indirect bandgap.[34] The indirect bandgap of the nanostructured $SrTiO_3$, Sr_2TiO_4 and $Sr_3Ti_2O_7$ was found to be 3.26 eV, 3.16 eV, and 3.11 eV respectively (Fig. 5a). A small change in the bandgap was observed with the change in the value of 'n' in SrO–$(SrTiO_3)_n$, which was consistent with the report by Chen *et al.*[35] wherein the authors also observed, through theoretical calculations, that the bandgap is affected by a small value with a slight change in the value of 'n' (n concerning $AO(ABO_3)_n$) in Mn-based Ruddlesden Popper-based perovskites. To calculate the band energy positions, XPS valence band spectra were recorded for $SrTiO_3$, Sr_2TiO_4, and $Sr_3Ti_2O_7$ (Fig. S4a–c, ESI†). The position of the valence band

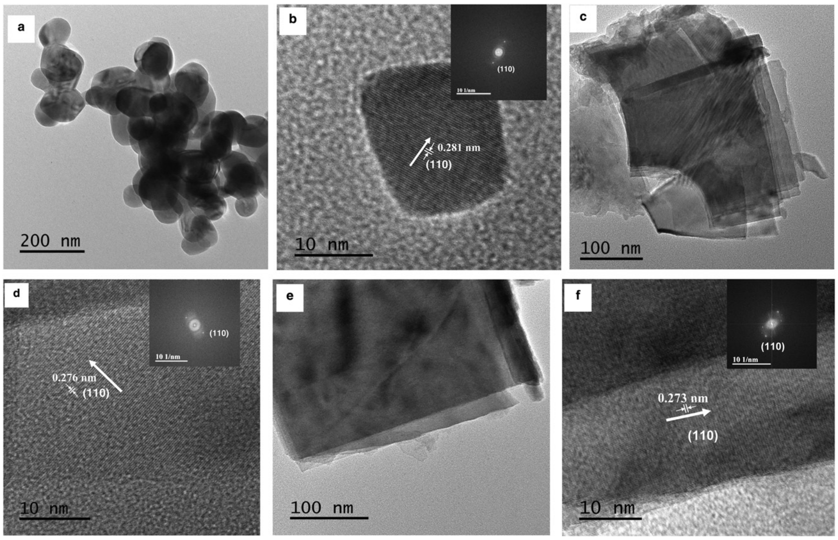

Fig. 4 TEM images of (a) $SrTiO_3$, (c) Sr_2TiO_4, and (e) $Sr_3Ti_2O_7$. HRTEM images of (b) $SrTiO_3$, (d) Sr_2TiO_4, and (f) $Sr_3Ti_2O_7$. The inset shows the corresponding reduced FFT of the HRTEM image.

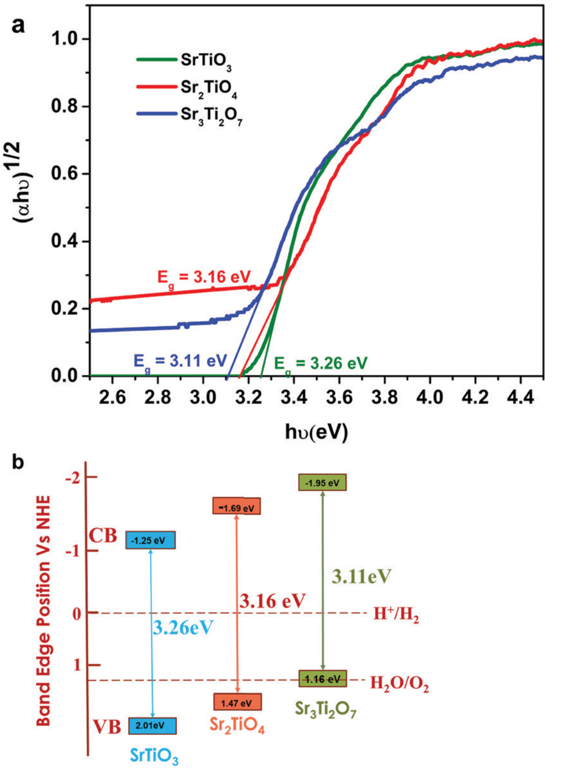

Fig. 5 (a) Tauc plot and (b) schematic showcasing the energy diagram for $SrTiO_3$, Sr_2TiO_4, and $Sr_3Ti_2O_7$.

maxima was observed to be 2.01, 1.47, and 1.16 eV for $SrTiO_3$, Sr_2TiO_4, and $Sr_3Ti_2O_7$ respectively. From the value of the band gap obtained from the Tauc plot and the valence band maxima obtained from the valence band spectra using XPS, the conduction band minima for $SrTiO_3$, Sr_2TiO_4, and $Sr_3Ti_2O_7$ were found to be −1.25, −1.69, and −1.95 eV (Fig. 5b). The conduction band positions for Sr_2TiO_4 and $Sr_3Ti_2O_7$ were observed to be more negative than $SrTiO_3$ indicating that the Ruddlesden–Popper phases are likely to exhibit superior catalytic activity towards hydrogen evolution compared with $SrTiO_3$.[36]

3.1 Photocatalytic H_2 evolution

The photocatalytic hydrogen evolution of nanostructured $SrTiO_3$ and $SrO(SrTiO_3)_n$ (n = 1 and 2) was studied by observing the amount of hydrogen evolved from an aqueous solution containing 0.25 M Na_2S and 0.35 M Na_2SO_3 (used as the hole-scavenger). The study was carried out in the absence of any metal co-catalyst to see the direct influence of the nature of the crystal structure on the photocatalytic performance of Sr–Ti–O based perovskites and Ruddlesden–Popper based oxides. At first, the experiments were carried out under dark conditions. No H_2 gas was observed in the absence of light. Temporal hydrogen evolution under light is shown in Fig. 6a and b. It was observed that the amount of H_2 evolved follows the order $Sr_3Ti_2O_7 > Sr_2TiO_4 > SrTiO_3$. Apparent quantum yield was calculated using eqn (3). The quantum yield obtained has been tabulated in Table 1. The recyclability test was performed on $Sr_3Ti_2O_7$ (exhibiting the evolution of the highest amount of hydrogen amongst the three oxides) to check its reusability. The recyclability test was examined for 12 h and each experimental

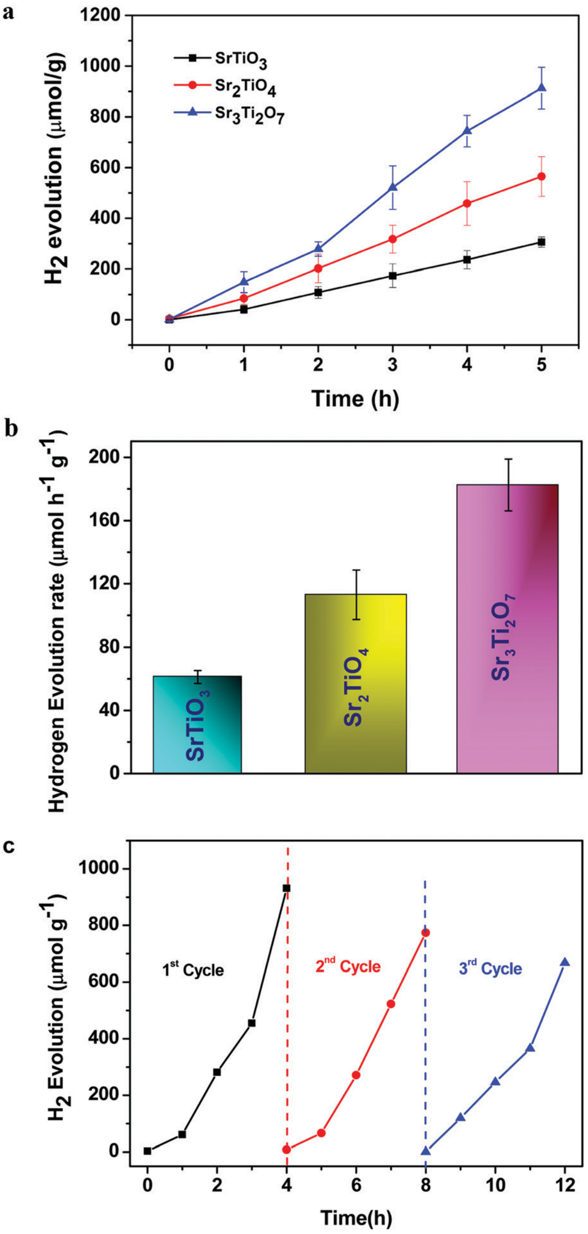

Fig. 6 (a) Plot showing the amount of hydrogen evolved per gram of the nanostructured catalyst ($SrTiO_3$, Sr_2TiO_4, and $Sr_3Ti_2O_7$). (b) The rate of hydrogen evolution per gram of the catalyst using nanostructures of $SrTiO_3$, Sr_2TiO_4, and $Sr_3Ti_2O_7$ as photocatalysts and (c) the recyclability test of $Sr_3Ti_2O_7$ for three consecutive cycles.

Table 1 Apparent quantum yield for hydrogen evolution using $SrTiO_3$, Sr_2TiO_4, and $Sr_3Ti_2O_7$ nanostructures as photocatalysts

Sample	n (amount of hydrogen gas evolved after 5 h of the reaction) (mol)	Apparent quantum yield (AQY) (%)
$SrTiO_3$	12.23×10^{-6}	0.018
Sr_2TiO_4 ($SrO(SrTiO_3)$)	22.6×10^{-6}	0.03
$Sr_3Ti_2O_7$ ($SrO(SrTiO_3)_2$)	36.5×10^{-6}	0.058

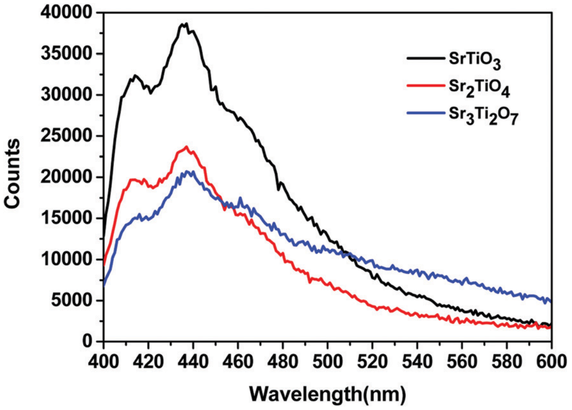

Fig. 7 Photoluminescence spectra of $SrTiO_3$, Sr_2TiO_4, and $Sr_3Ti_2O_7$.

cycle was carried out for 4 h (Fig. 6c). The oxide was centrifuged and washed with water between each cycle. A slight decrease in the rate of H_2 evolution was observed for three cycles. The stability of the catalyst was checked after the recyclability test of 12 h through PXRD (Fig. S5, ESI†). It was observed that the crystal structure of the catalyst remained unchanged after reusability. No additional peaks corresponding to any impurity were observed suggesting that the oxide was stable after 12 h.

To ascertain the reason for the observed trend for the photocatalytic hydrogen evolution, photoluminescence (PL) and time-resolved photoluminescence studies were carried out for the three oxides. Fig. 7 shows the photoluminescence spectra for all the samples. Here, the samples were excited at a wavelength of 380 nm, and the emission spectra were recorded in the range of 395–700 nm. All the samples showed PL emission in the violet-blue region with a peak centered at 414 nm and 436 nm. It has been reported[37] that the photoluminescence for $SrTiO_3$ based oxides arises mostly due to a recombination of the electrons and holes that are trapped in the intermediate states (present within the bandgap). These intermediate states arise as a result of distortion, oxygen vacancies, *etc.* It has also been reported[37] that the emission in the violet-blue region occurs due to the presence of a surface or shallow defects which may arise due to oxygen vacancies. Oxygen vacancies are also known to affect the catalytic behavior of oxides.[5,38] The presence of a controlled concentration of defects (oxygen vacancies) is known to increase the photocatalytic efficiency of $SrTiO_3$ towards hydrogen evolution.[39] The oxygen vacancies act as electron donors which either result in an increased charge transport or a shift in the Fermi level towards the conduction band.[39] Such a phenomenon is likely to improve the charge separation behavior of the oxide. In our studies, the presence of defect/oxygen vacancies was also confirmed by Raman and XPS studies. In addition to the presence of defects, it was also observed that the PL emission, corresponding to the defect, decreased in the following order $SrTiO_3 > Sr_2TiO_4 > Sr_3Ti_2O_7$. With the same excitation energy and no significant changes in the optical bandgap of the oxides, the decrease in the PL emission can be related to a decrease in the recombination of electron and hole pairs giving rise to radiative emission. To further investigate the lifetime of photo-induced charge carriers, time-resolved photoluminescence decay spectra were recorded. The data was fitted using eqn (1) and the average lifetime (τ_{avg}) was calculated using eqn (2). Fig. 8a–c show the second exponential decay fit of the time-resolved PL of the three oxides. The parameters obtained after fitting are listed in Table 2. The average lifetime was found to follow the order $Sr_3Ti_2O_7 > Sr_2TiO_4 > SrTiO_3$, for the Sr–Ti–O system. From the values obtained for τ_{avg} (ns), it can be concluded that the recombination of photo-induced charge carriers is delayed for Ruddlesden–Popper based oxides (Sr_2TiO_4 and $Sr_3Ti_2O_7$) compared with $SrTiO_3$. The longer lifetime implies

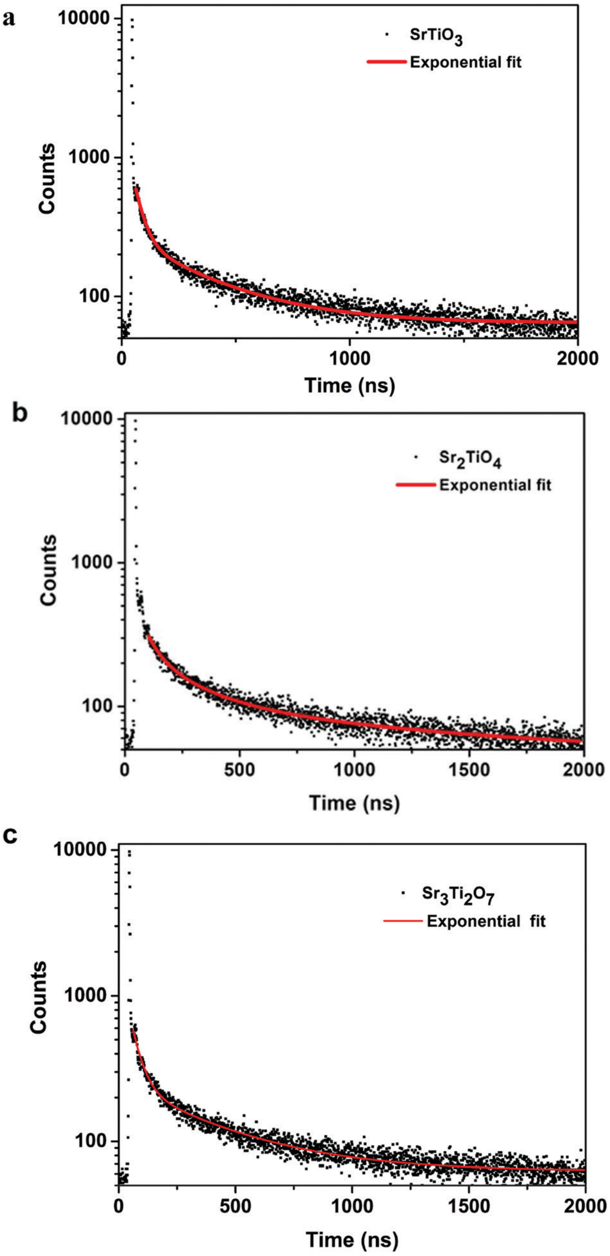

Fig. 8 Time-resolved photoluminescence decay of (a) $SrTiO_3$, (b) Sr_2TiO_4 and (c) $Sr_3Ti_2O_7$.

Table 2 Parameters obtained after exponential fitting of the decay curves for $SrTiO_3$, Sr_2TiO_4, and $Sr_3Ti_2O_7$

Sample	A_1	τ_1 (ns)	A_2	τ_2 (ns)	Average lifetime τ_{avg} (ns)
$SrTiO_3$	1800	37.7 ± 1.0	213	351 ± 8.6	202
Sr_2TiO_4	1646	38.0 ± 1.2	198	367 ± 8.8	215
$Sr_3Ti_2O_7$	1619	40.3 ± 1.0	194	392 ± 10	230

that a large number of photo-induced electrons could reach the surface of the catalysts which would be captured by the H^+ ions. Thus, the longer lifetime of the photo-induced charge carriers for $Sr_3Ti_2O_7$ further supports the increased photocatalytic properties of $Sr_3Ti_2O_7$. The presence of interlayers (SrO layer in our study) results in a reduction of the recombination of photo-generated charge carriers by separation of the electrons and holes thereby enhancing the photocatalytic water splitting reaction.[40]

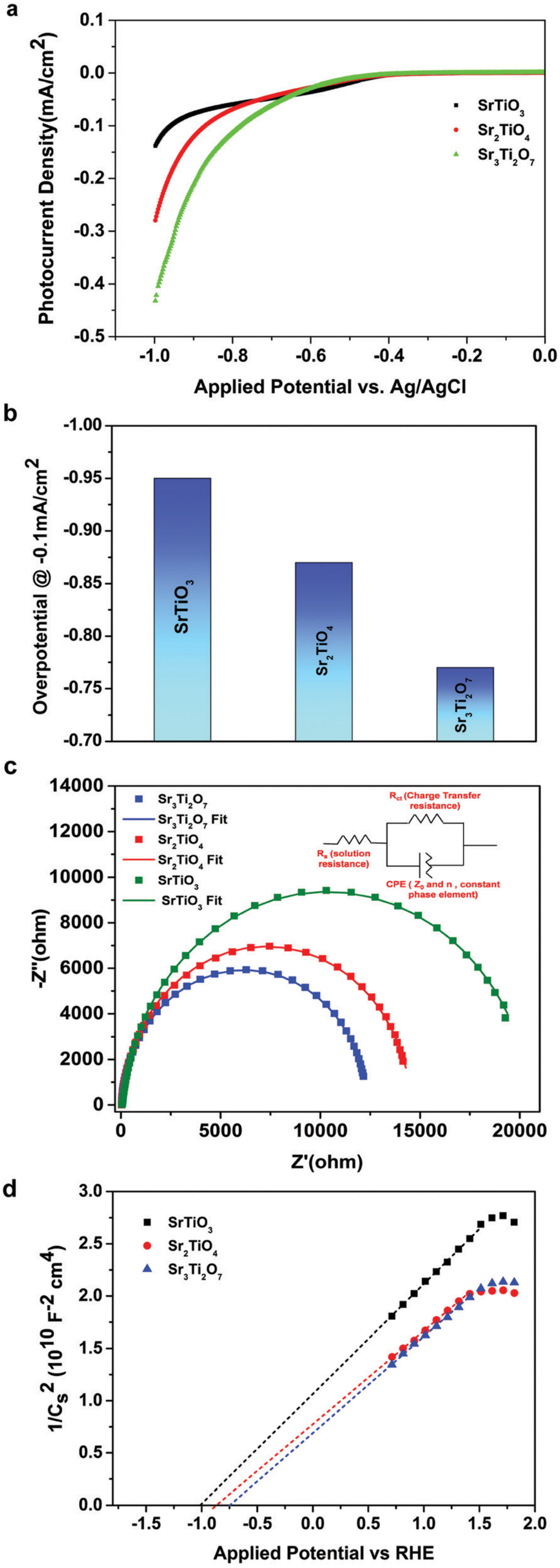

Fig. 9 (a) Photocurrent density, (b) overpotential, (c) Nyquist plot and (d) Mott–Schottky plot for $SrTiO_3$, Sr_2TiO_4, and $Sr_3Ti_2O_7$.

To further evaluate the charge transfer behavior of the three oxides in the presence of light, photoelectrochemical studies were carried out. The photocurrent density (Fig. 9a) was found to be the highest for $Sr_3Ti_2O_7$. The onset potential was observed to be ~ -0.40 V *vs.* Ag/AgCl, which is nearly the same for all three samples. The overpotential for the hydrogen evolution reaction (HER) for the three oxides was evaluated from the current–voltage curve at -0.1 mA cm^{-2} *vs.* Ag/AgCl (Fig. 9b). The overpotential was found to follow the order $SrTiO_3 > Sr_2TiO_4 > Sr_3Ti_2O_7$ for the Sr–Ti–O system. Fig. 9c shows Nyquist plots for the three oxides. Based on R_{ct} (charge transfer resistance), R_s (solution resistance), and a constant phase element with impedance, which is related to the angular frequency of the applied potential, ω (using eqn (5)),

$$Z = \frac{Z_0}{(i\omega)^n} \tag{5}$$

where Z_0 is a constant, and the value of n ranges as follows: $0 < n < 1$, $i = \sqrt{-1}$, the curve was fit to an equivalent circuit, shown in the inset of Fig. 9c. The parameters obtained after the fitting are tabulated in Table 3. The charge transfer resistance originating as a result of the ionic and electronic resistance across the electrode–electrolyte interface, R_{ct}, were observed to follow the order: $Sr_3Ti_2O_7 < Sr_2TiO_4 < SrTiO_3$. Mott–Schottky studies in the presence of light (Fig. 9d) were carried out to calculate the charge carrier density using the following equation:

$$\frac{1}{C^2} = \frac{2}{\varepsilon\varepsilon_0 A^2 e N_d}\left(V - V_{fb} - \frac{k_B T}{e}\right) \tag{6}$$

where C is the interfacial capacitance, ε is the dielectric constant of the material (250, 38, and 50 for $SrTiO_3$ Sr_2TiO_4 and $Sr_3Ti_2O_7$ respectively),[41] ε_0 is the permittivity of vacuum (8.854×10^{-12} F m^{-1}), e is the fundamental charge (1.602×10^{-19} C), A is the area of the electrode (1 cm^2), N_d is the charge carrier density, V is the applied potential, k_B is Boltzmann's constant, and T is the temperature. The positive slope of the plot suggests the n-type semiconducting behavior of the oxides. The n-type behavior in $SrTiO_3$ arises due to the presence of

Table 3 Parameters obtained after fitting the Nyquist plot

Sample	R_{ct} (kΩ)	R_s (Ω)	CPE (μmho)	n (in constant phase element)
$SrTiO_3$	20.6	36.5	16.0	0.940
Sr_2TiO_4	14.5	28.4	12.5	0.973
$Sr_3Ti_2O_7$	12.3	26.5	12.1	0.974

oxygen vacancies.[42,43] The charge carrier density N_d was calculated from the slope using eqn (7).

$$\text{Slope} = \frac{2}{\varepsilon\varepsilon_0 e \times N_d} \qquad (7)$$

The slope was observed to be 1.07×10^{10} F^{-2} cm^4 V^{-1}, 0.88×10^{10} F^{-2} cm^4 V^{-1} and 0.87×10^{10} F^{-2} cm^4 V^{-1} for $SrTiO_3$ Sr_2TiO_4 and $Sr_3Ti_2O_7$ respectively. Thus, N_d was calculated to be 5.3×10^{19} cm^{-3}, 4.2×10^{20} cm^{-3} and 3.2×10^{20} cm^{-3} for $SrTiO_3$ Sr_2TiO_4 and $Sr_3Ti_2O_7$ respectively. The charge carrier density was found to be in the following order: $Sr_2TiO_4 \approx Sr_3Ti_2O_7 > SrTiO_3$ consistent with the photocatalytic performance of the oxide.

Thus, from the trend observed for the photocatalytic hydrogen evolution there are a few interesting observations. One, the photocatalytic hydrogen evolution increases with the introduction of the SrO layer *i.e.* when comparing $SrTiO_3$ with Sr_2TiO_4 ($SrO(SrTiO_3)$). The SrO layer in Ruddlesden–Popper based layered perovskites[44] is responsible for the dissociation of water. The oxygen site (apical oxygen) in $SrTiO_3$ of Ruddlesden–Popper based layered perovskites favors the adsorption of hydrogen enabling its recombination with other adsorbed hydrogen to form H_2. Wei *et al.*[45] also observed that insertion of the SrO layer in $SrTaO_2N$ to form Sr_2TaO_3N (a Ruddlesden–Popper based oxynitride) resulting in the improved photocatalytic performance of the oxynitride. Second, with the increase in the $SrTiO_3$ perovskite unit in Ruddlesden–Popper based layered perovskites *i.e.* on comparing Sr_2TiO_4 and $Sr_3Ti_2O_7$, the photocatalytic activity was found to increase for $Sr_3Ti_2O_7$. For photocatalytic water splitting, the active sites in Ruddlesden–Popper based layered perovskites are the B-site cations (Ti in Sr–Ti–O based systems), AO layers (SrO layer in Sr–Ti–O based systems), and defects arising due to oxygen vacancies. This arrangement of layers is known to suppress the charge carrier recombination, as evident from time-resolved photoluminescence studies, and promote charge carrier transfer, as evident from a decrease in charge transfer resistance.

Based on the study, it is also to be noted there are two important synergistic factors that affect the photocatalytic behavior of the oxides: (a) crystal structure and the arrangement of atoms, and (b) the presence of defects (oxygen vacancies). Thus, synergism in the role of the SrO layer and the $SrTiO_3$ perovskite unit along with the layered morphology, low crystallite size, and presence of defects (oxygen vacancies), is presumed to have resulted in an improved photocatalytic performance for Ruddlesden–Popper based layered perovskite. This improved performance was evident from the reduced overpotential, low charge transfer resistance, and high charge carrier density for Ruddlesden–Popper based layered perovskites. Hence, the appropriate choice of the crystal structure from a series could result in attaining the desired factors required for designing an efficient catalyst for photocatalytic HER.

4. Conclusions

We have successfully synthesized three members of the Sr–Ti–O system *viz.* $SrTiO_3$, Sr_2TiO_4, and $Sr_3Ti_2O_7$ using the combination of a polymeric citrate precursor and a hydrothermal method. $SrTiO_3$ was observed to crystallize into a cubic structure and possessed cube-like morphology. Sr_2TiO_4 and $Sr_3Ti_2O_7$ were found to crystallize in a tetragonal crystal structure. Sheet-like morphology was observed for these two oxides. We have demonstrated photocatalytic hydrogen evolution activity for these three nanostructured oxides. All three structures were found to be active photocatalysts under a full range of light irradiation and in the absence of any co-catalyst. We observed that the nanocubes of $SrTiO_3$ (perovskite cubic crystal structure) were less active for the photocatalytic HER than layered Sr_2TiO_4 and $Sr_3Ti_2O_7$ (tetragonal, Ruddlesden–popper structure). Synergism of many factors which included the presence of a SrO layer, $SrTiO_3$ unit, layered morphology, low crystallite size, and defects is attributed to the observed photocatalytic performance of the Ruddlesden–popper structure in comparison to cubic perovskite $SrTiO_3$. Thus, the findings in our study highlight the influence of the Ruddlesden–Popper crystal structure on the hydrogen evolution efficiency of perovskite oxides. The study opens a strategic approach based on choosing the crystal structure while designing highly efficient catalysts.

Conflicts of interest

There are no conflicts of interest to declare.

Acknowledgements

A. V. thanks INST, Mohali for the fellowship. SV thanks CSIR (01(2943)/18-EMR-II), Govt. of India for funding.

References

1 K. Maeda, K. Teramura, D. Lu, T. Takata, N. Saito, Y. Inoue and K. Domen, *Nature*, 2006, **440**, 295.
2 H. Tong, S. Ouyang, Y. Bi, N. Umezawa, M. Oshikiri and J. Ye, *Adv. Mater.*, 2012, **24**, 229–251.
3 Y.-F. Li, Z.-P. Liu, L. Liu and W. Gao, *J. Am. Chem. Soc.*, 2010, **132**, 13008–13015.
4 S. Ouyang and J. Ye, *J. Am. Chem. Soc.*, 2011, **133**, 7757–7763.
5 A. Kumar and V. Krishnan, *Adv. Funct. Mater.*, 2021, **31**, 2009807.
6 N. M. Flores, U. Pal, R. Galeazzi and A. Sandoval, *RSC Adv.*, 2014, **4**, 41099–41110.
7 L. Zhang, T. Xu, X. Zhao and Y. Zhu, *Appl. Catal., B*, 2010, **98**, 138–146.

8 Y. Liu, B. Huang, Y. Dai, X. Zhang, X. Qin, M. Jiang and M.-H. Whangbo, *Catal. Commun.*, 2009, **11**, 210–213.

9 S. Ouyang, N. Kikugawa, D. Chen, Z. Zou and J. Ye, *J. Phys. Chem. C*, 2009, **113**, 1560–1566.

10 T. A. Kandiel, A. Feldhoff, L. Robben, R. Dillert and D. W. Bahnemann, *Chem. Mater.*, 2010, **22**, 2050–2060.

11 T. Li, H. Cai, C. Li, X. Liu and F. Huang, *Front. Chem.*, 2020, **8**, 351.

12 S. Chen, D. Huang, P. Xu, W. Xue, L. Lei, M. Cheng, R. Wang, X. Liu and R. Deng, *J. Mater. Chem. A*, 2020, **8**, 2286–2322.

13 J. Cai, A. Cao, Z. Wang, S. Lu, Z. Jiang, X.-Y. Dong, X. Li and S.-Q. Zang, *J. Mater. Chem. A*, 2021, **9**, 13890–13897.

14 S. Kumar, A. Kumar, A. Kumar and V. Krishnan, *Catal. Rev.*, 2020, **62**, 346–405.

15 H. Mai, D. Chen, Y. Tachibana, H. Suzuki, R. Abe and R. A. Caruso, *Chem. Soc. Rev.*, 2021, **50**, 13692–13729.

16 G. Zhang, G. Liu, L. Wang and J. T. S. Irvine, *Chem. Soc. Rev.*, 2016, **45**, 5951–5984.

17 A. Kumar, A. Kumar and V. Krishnan, *ACS Catal.*, 2020, **10**, 10253–10315.

18 T. Kimijima, K. Kanie, M. Nakaya and A. Muramatsu, *Appl. Catal., B*, 2014, **144**, 462–467.

19 P.-L. Hsieh, G. Naresh, Y.-S. Huang, C.-W. Tsao, Y.-J. Hsu, L.-J. Chen and M. H. Huang, *J. Phys. Chem. C*, 2019, **123**, 13664–13671.

20 A. Vijay and S. Vaidya, *ACS Appl. Nano Mater.*, 2021, **4**, 3406–3415.

21 T. Oshima, T. Yokoi, M. Eguchi and K. Maeda, *Dalton Trans.*, 2017, **46**, 10594–10601.

22 K.-i Shimizu, Y. Tsuji, T. Hatamachi, K. Toda, T. Kodama, M. Sato and Y. Kitayama, *Phys. Chem. Chem. Phys.*, 2004, **6**, 1064–1069.

23 X. Sun, Y. Xie, F. Wu, H. Chen, M. Lv, S. Ni, G. Liu and X. Xu, *Inorg. Chem.*, 2015, **54**, 7445–7453.

24 H. Zhang, S. Ni, Y. Mi and X. Xu, *J. Catal.*, 2018, **359**, 112–121.

25 K. Yamada, H. Suzuki, R. Abe and A. Saeki, *J. Phys. Chem. Lett.*, 2019, **10**, 1986–1991.

26 H. Jeong, T. Kim, D. Kim and K. Kim, *Int. J. Hydrogen Energy*, 2006, **31**, 1142–1146.

27 X. Sun, Y. Xie, F. Wu, H. Chen, M. Lv, S. Ni, G. Liu and X. Xu, *Inorg. Chem.*, 2015, **54**, 7445–7453.

28 Y. Liu, L. Xie, Y. Li, R. Yang, J. Qu, Y. Li and X. Li, *J. Power Sources*, 2008, **183**, 701–707.

29 W. G. Nilsen and J. G. Skinner, *J. Chem. Phys.*, 1968, **48**, 2240–2248.

30 S. Banerjee, D.-I. Kim, R. D. Robinson, I. P. Herman, Y. Mao and S. S. Wong, *Appl. Phys. Lett.*, 2006, **89**, 223130.

31 R. Viennois, P. Hermet, D. Machon, M. M. Koza, D. Bourgogne, B. Fraisse, A. P. Petrović and D. Maurin, *J. Phys. Chem. C*, 2020, **124**, 27882–27893.

32 A. Dias, J. I. Viegas and R. L. Moreira, *J. Alloys Compd.*, 2017, **725**, 77–83.

33 S. Kamba, P. Samoukhina, F. Kadlec, J. Pokorný, J. Petzelt, I. M. Reaney and P. L. Wise, *J. Eur. Ceram. Soc.*, 2003, **23**, 2639–2645.

34 C.-H. Lee, N. J. Podraza, Y. Zhu, R. F. Berger, S. Shen, M. Sestak, R. W. Collins, L. F. Kourkoutis, J. A. Mundy, H. Wang, Q. Mao, X. Xi, L. J. Brillson, J. B. Neaton, D. A. Muller and D. G. Schlom, *Appl. Phys. Lett.*, 2013, **102**, 122901.

35 A. Chen, X. Zhang, Z. Zhang, S. Yao and Z. Zhou, *J. Mater. Chem. A*, 2019, **7**, 11530–11536.

36 H. Chen and X. Xu, *Appl. Catal., B*, 2017, **206**, 35–43.

37 A. E. Souza, G. T. A. Santos, B. C. Barra, W. D. Macedo, S. R. Teixeira, C. M. Santos, A. M. O. R. Senos, L. Amaral and E. Longo, *Cryst. Growth Des.*, 2012, **12**, 5671–5679.

38 T. Zheng, W. Sang, Z. He, Q. Wei, B. Chen, H. Li, C. Cao, R. Huang, X. Yan, B. Pan, S. Zhou and J. Zeng, *Nano Lett.*, 2017, **17**, 7968–7973.

39 H. Tan, Z. Zhao, W.-B. Zhu, E. N. Coker, B. Li, M. Zheng, W. Yu, H. Fan and Z. Sun, *ACS Appl. Mater. Interfaces*, 2014, **6**, 19184–19190.

40 Z. Liang, K. Tang, Q. Shao, G. Li, S. Zeng and H. Zheng, *J. Solid State Chem.*, 2008, **181**, 964–970.

41 W. Kwestroo and H. A. M. Paping, *J. Am. Ceram. Soc.*, 1959, **42**, 292–299.

42 P. Calvani, M. Capizzi, F. Donato, S. Lupi, P. Maselli and D. Peschiaroli, *Phys. Rev. B: Condens. Matter Mater. Phys.*, 1993, **47**, 8917–8922.

43 O. N. Tufte and P. W. Chapman, *Phys. Rev.*, 1967, **155**, 796–802.

44 Y. Zhu, H. A. Tahini, Z. Hu, J. Dai, Y. Chen, H. Sun, W. Zhou, M. Liu, S. C. Smith, H. Wang and Z. Shao, *Nat. Commun.*, 2019, **10**, 149.

45 S. Wei and X. Xu, *Appl. Catal., B*, 2018, **228**, 10–18.